Journal of Materials Chemistry A

PAPER

View Article Online
View Journal | View Issue

Cite this: J. Mater. Chem. A, 2018, 6, 17587

Water adsorption at zirconia: from the ZrO_2(111)/Pt_3Zr(0001) model system to powder samples†

Peter Lackner,[a] Jan Hulva,[a] Eva-Maria Köck,[b] Wernfried Mayr-Schmölzer,[ac] Joong Il J. Choi,‡[a] Simon Penner,[b] Ulrike Diebold,[a] Florian Mittendorfer,[ac] Josef Redinger,[ac] Bernhard Klötzer,[b] Gareth S. Parkinson[a] and Michael Schmid *[a]

We present a comprehensive study of water adsorption and desorption on an ultrathin trilayer zirconia film using temperature programmed desorption (TPD), X-ray photoelectron spectroscopy (XPS), as well as scanning tunneling microscopy (STM) at different temperatures. The saturation coverage is one H_2O per surface Zr atom, with about 12% dissociation. The monolayer TPD peak (180 K, desorption barrier 0.57 ± 0.04 eV) has a tail towards higher temperatures, caused by recombinative desorption from defect sites with dissociated water. STM shows that the defects with the strongest H_2O adsorption are found above subsurface dislocations. Additional defect sites are created by multiple water adsorption/desorption cycles; these water-induced changes were also probed by CO_2 TPD. Nevertheless, the defect density is much smaller than in previous studies of H_2O/ZrO_2. To validate our model system, transmission Fourier-transform infrared absorption spectroscopy (FTIR) studies at near-ambient pressures were carried out on monoclinic zirconia powder, showing comparable adsorption energies as TPD on the ultrathin film. The results are also compared with density functional theory (DFT) calculations, which suggest that sites with strong H_2O adsorption contain twofold-coordinated oxygen.

Received 4th May 2018
Accepted 5th August 2018

DOI: 10.1039/c8ta04137g

rsc.li/materials-a

1 Introduction

Many technological applications of zirconia (ZrO_2; pure or yttrium-doped, then known as yttria-stabilized zirconia YSZ) involve interaction with water. Examples are internal steam reforming in solid oxide fuel cells,[1] catalysis,[2] gas sensors,[3] or applications as biocompatible material.[4] However, little is known about the interaction of water with ZrO_2 surfaces on a fundamental level, which is mostly due to a lack of suitable samples. This is quite different for other oxides.[5–7] Water adsorbs only weakly on many defect-free oxide surfaces; in ultra-high vacuum (UHV) it then desorbs below room temperature (RT), typically at 160–250 K.[8–10] H_2O can bind more strongly to surfaces with defects, as shown for the prototypical example of rutile TiO_2(110).[11,12] In these cases, H_2O dissociates into an OH group, which fills an oxygen vacancy, and into a hydrogen atom, which binds to surface oxygen and forms a second OH group. On TiO_2, these OH groups are stable up to ≃490 K.[13] On defect-free oxide surfaces, water can bind strongly if the surface termination includes highly reactive cations. It can then readily dissociate, *e.g.* on α-Cr_2O_3(001),[14] α-Fe_2O_3(012),[15] and on oxides of the alkaline earths,[16] including CaO-terminated $Ca_3Ru_2O_7$(001).[17] On RuO_2(110),[18] PdO(101),[19] and Fe_3O_4(001),[20] water binds to coordinatively unsaturated cations and forms partially dissociated structures stabilized by hydrogen bonds.

Such detailed studies are not yet available for water on ZrO_2; only few reports on H_2O adsorption can be found in the literature. On powder materials, very high adsorption enthalpies were reported for low H_2O coverages (≳2 eV on monoclinic and ≈1.5 eV on tetragonal ZrO_2), decreasing to liquid-water like binding (0.45 eV) at coverages around 2–4 H_2O/nm^2.[21,22] Moderate values (≈0.6 eV, derived from a TPD peak at 240–250 K) were reported for H_2O on oxidized polycrystalline Zr, *i.e.*, a hydroxylated and, possibly, substoichiometric film.[23] To the best of our knowledge, there are no studies of H_2O adsorption on well-defined single-crystalline ZrO_2 surfaces so far. This is related to the fact that single crystals of pure ZrO_2 grown from the melt exhibit phase transformations upon cooling, thus only crystals of doped zirconia (*e.g.*, YSZ) are available; these retain the high-temperature cubic phase. The surface chemistry of YSZ is much more complex than that of pure ZrO_2, however, as shown for adsorption of H_2O,[24] hydrogen,[25] or CO and CO_2.[26] Therefore, the investigation of pure ZrO_2, which is needed as a starting point of a well-grounded fundamental understanding, has to rely on thin films.

[a]Institute of Applied Physics, TU Wien, 1040 Vienna, Austria. E-mail: schmid@iap.tuwien.ac.at; Fax: +43 1 58801 13499; Tel: +43 1 58801 13401

[b]Institute of Physical Chemistry, University of Innsbruck, 6020 Innsbruck, Austria

[c]Center for Computational Materials Science, TU Wien, 1040 Vienna, Austria

† Electronic supplementary information (ESI) available. See DOI: 10.1039/c8ta04137g

‡ Present address: Center for Nanomaterials and Chemical Reactions, Institute for Basic Science (IBS), Daejeon 305-701, Republic of Korea.

Well-defined, pure zirconia surfaces can be created as thin films, which have the additional advantage that the surface of the otherwise perfectly insulating zirconia can be probed by techniques that rely on electron transfer, such as scanning tunneling microscopy (STM). Such ZrO_2 films can be obtained by deposition of Zr in oxygen background gas.[27–30] Temperature programmed desorption (TPD) studies on 7 ML-thick ZrO_2 films on Pt(111) show three desorption peaks (190 K, 275 K, and 370 K with adsorption energies 0.46, 0.68, and 0.92 eV, respectively).[31,32] The authors suggested that water in the low-temperature peak binds molecularly while the rest is in dissociated form. The two desorption peaks at higher temperatures were assigned to defect sites.

Ultra-thin ZrO_2 films can also be prepared by oxidation of suitable Zr alloys, Pt_3Zr[33,34] or Pd_3Zr.[35] This approach has the advantages of better homogeneity of the films, especially a more uniform thickness, and is also less susceptible to impurity adsorption as these alloys are much less reactive than pure Zr. By a combination of STM, Auger and photoelectron spectroscopy, as well as DFT, it has been shown that the films grown by oxidation of Pt_3Zr or Pd_3Zr consist of one trilayer (O–Zr–O), structurally equivalent to a trilayer of cubic ZrO_2(111), but with additional distortions.[33,35,36] The oxide film is created by Zr diffusion to the surface when annealing in oxygen. In the case of Pt_3Zr, diffusion of Zr in the alloy is slow, thus a Zr-depleted Pt region remains below the oxide. The slightly smaller interatomic distance of Pt (0.2775 nm) in comparison with Pt_3Zr (0.281 nm) leads to a contraction of the Pt layer below the oxide film. As a consequence, misfit dislocations form between the Pt layer at the interface and the alloy below. These subsurface dislocations are visible as bright ridges in STM. The atoms in the ultra-thin ZrO_2 trilayer above the Pt layer are well ordered with an average in-plane distance of 350 pm and exhibit strong vertical buckling. These height differences are related to the $(\sqrt{19} \times \sqrt{19})R23.4^\circ$ superstructure (1.2 nm periodicity), resulting from the different lattice constants of the oxide and the underlying Pt layer. The unit cell of the superstructure includes 12 Zr atoms, which are accessible to adsorbates due to the large distance between the O atoms in the layer above, and the low interlayer distance between the O and Zr layers.[33] A model of the superstructure as calculated by density functional theory (DFT) is presented in the DFT chapter below.

In this work we present an extensive study of water on ZrO_2 ultra-thin films grown by oxidation of Pt_3Zr(0001) single crystals. We combine TPD, X-ray photoelectron spectroscopy (XPS), and STM with DFT calculations and show how adsorbed H_2O behaves on zirconia trilayers. Furthermore, we performed Fourier-transform infrared spectroscopy (FTIR) absorption measurements of H_2O on monoclinic ZrO_2 powder, to test the validity of the ultra-thin oxide as a model system for technological zirconia surfaces.

2 Experimental and computational methods

2.1 Ultra-high vacuum setup

UHV experiments were conducted in three different systems. Temperature-programmed desorption (TPD) and X-ray photoelectron spectroscopy (XPS) measurements were performed in a UHV chamber described thoroughly elsewhere.[37] This system features a LHe flow cryostat, which can cool the sample to 20 K. The base pressure in the chamber was below 10^{-10} mbar. A Pt_3Zr(0001) single crystal (6 mm diameter) was wrapped with Ta ribbons at the circumference; these were spot-welded to thicker Ta bars leading directly to the cryostat to ensure good thermal contact. A K-type thermocouple was spot-welded directly to the backside of the crystal for accurate temperature measurements. No sample plate was used. The chamber includes a molecular-beam setup for precise gas dosing (such as D_2O) with a sharp top-hat profile in a circular area with a diameter of 3.2 mm.[37] This allows us to perform TPD and XPS measurements with water sticking exclusively to the center of the well-prepared crystal surface; there is no influence from water on the Ta ribbons or from the edges of the crystal. Furthermore, the molecular beam provides accurate gas doses. Since the sticking coefficient equals unity, the coverage can be given in monolayers or molecules per trilayer Zr atom. We define one monolayer (ML) as one water molecule per surface Zr atom (9.5 nm^{-2}, corresponding to 12 molecules per $(\sqrt{19} \times \sqrt{19})R23.4^\circ$ ZrO_2 trilayer unit cell). For XPS, a monochromatised Al Kα (1486.7 eV) X-ray source was used. All XPS measurements were done at 100 K and in normal emission. To reduce the influence of the residual gas on the TPD data, experiments in this chamber (TPD, XPS) were done with D_2O, while H_2O was used everywhere else.

Scanning tunneling microscopy (STM) measurements were performed in two different chambers. Low-temperature STM was performed using an Omicron LT-STM in a two-chamber UHV system with a base pressure below 1.5×10^{-11} mbar in the STM chamber, and 4×10^{-11} mbar in the preparation chamber. During the measurement the sample was cooled to 78 K. Room-temperature STM measurements were preformed using an Omicron μ-STM in a chamber described in ref. 33. This two-chamber system is divided into a measurement chamber ($p_{base} < 7 \times 10^{-11}$ mbar) and a preparation chamber ($p_{base} < 10^{-10}$ mbar). STM data were acquired in constant-current mode with electrochemically etched W tips. We report sample voltages for the STM images, thus positive voltages refer to tunneling into the unoccupied states of the surface. All STM images were corrected for creep of the piezo scanner as described in ref. 35.

2.2 *In situ* FTIR spectroscopy setup

Fourier-transform infrared absorption spectroscopy (FTIR) measurements of ZrO_2 powder were recorded in transmission mode on an Agilent Cary 660 spectrometer with a mid-infrared source and a deuterated triglycine sulfate (DTGS) detector. The powder samples were pressed into thin pellets using a pressure equivalent to 1.5 t on a 0.8 cm^2 area (sample diameter 10 mm, mass about 20 mg) and subsequently placed inside a home-made *in situ*/*operando* reactor cell.[38] This cell provides an inert all-quartz surrounding of the sample in the heated area. *In situ* measurements can be performed up to 1273 K under flowing and static conditions. Also, vacuum with a minimum pressure

of 10^{-7} mbar is obtainable. The window material, BaF_2, provides access to wave numbers above 800 cm^{-1}. Experiments in flowing mode were performed using He as carrier gas. In static mode, water vapor was admitted stepwise to the evacuated cell. The water reservoir was degassed beforehand to remove dissolved atmospheric gases, in particular CO_2. All reported spectra are corrected by the spectrum of the dry pre-oxidized oxide pellet at room temperature and under vacuum, prior to exposure to water.

2.3 Sample preparation

The $Pt_3Zr(0001)$ single crystals used for UHV studies were grown, cut and polished by MaTecK (Germany). The cleaning procedure was based on the recipe from ref. 33, with slight changes: cycles of sputtering (2 keV Ne^+ ions in the XPS/TPD chamber, or Ar^+ in the STM chambers; 20 min, current density $\approx$ 4 μA cm^{-2}) and annealing (1175 K, 10 min). The last sputter cycle was applied during a linear temperature ramp from 680 K to 380 K in 20 min to reduce the density of steps and eliminate half-steps.[33] The cleanliness of the sample was checked with XPS. An ultra-thin ZrO_2 trilayer (O–Zr–O) was prepared by first annealing in oxygen ($p = 1 \times 10^{-7}$ mbar, 680 K, 10 min) and then in UHV (1205 K, 30 min). The first annealing step causes Zr diffusion to the surface and oxidation, but results in poorly ordered structures. In the second step the oxide forms a well-ordered ultra-thin O–Zr–O trilayer; three-dimensional (3D) ZrO_2 clusters disappear by spreading out and/or dissolving into the bulk. In the present study, the final annealing temperature was set higher than in ref. 33 and 36 to reduce the amount of ZrO_2 clusters. Although both, the annealing temperature and the annealing time, were increased compared to the recipe from Antlanger *et al.*,[33] the film did not break up, as verified by CO TPD, which did not show any indications of a CO signal from adsorption on the substrate.[36] The resulting sample is a trilayer of $ZrO_2(111)$ on a Zr-depleted $Pt_3Zr(0001)$ surface. In the following this is shortened to "ZrO_2/Pt_3Zr". For the LT-STM measurements, the sample could be heated to only 1160 K; nevertheless, STM showed large areas free of ZrO_2 clusters (Fig. S1 of the ESI†). The preparation procedures are summarized in the ESI (Table S1†).

Both D_2O (TPD and XPS measurements) and H_2O (STM measurements) were purified *via* several freeze–pump–thaw cycles. All gases were checked for cleanliness with mass spectrometers. For TPD and XPS measurements, water was dosed using the molecular-beam doser (see above), for STM measurements water was dosed by back-filling of the chamber, making the given doses less accurate.

For the FTIR experiments, commercial powder of monoclinic ZrO_2 (zirconium (IV) oxide, 99.978%; Alfa Aesar) was used. To guarantee a well-defined, carbon- and water-depleted and sufficiently (for the subsequent experimental temperatures) sintered material, the sample was heated inside the *in situ* setup in pure, dry oxygen up to 1273 K and held for one hour prior to the water adsorption experiments. The sample was routinely checked by XRD for structural changes after annealing and after the water adsorption experiments. After the pretreatment, the surface area was determined as 2 m^2 g^{-1} (ZrO_2) by nitrogen adsorption at 77 K according to the Brunauer–Emmett–Teller (BET) method. For BET measurements, a Quantachrome Nova 2000 Surface Area and Pore Size Analyzer was used. Gases were supplied by Messer (O_2 5.0, He 5.0). The cooling trap for removing residual moisture from O_2 was set at ~153 K.

2.4 Computational methods

The DFT calculations were performed with the Vienna *Ab initio* Simulation Package (VASP) using the projector augmented wave framework.[39] Earlier work has shown that dispersion effects can play a substantial role in the correct description of both the metal–zirconia[33] and the solid–water interface.[16,40,41] Therefore, the van-der-Waals corrected so-called optB86b[42,43] functional was used to properly treat dispersion effects, employing the formalism introduced by Dion *et al.*[44] Due to the large size of the $(\sqrt{19} \times \sqrt{19})R23.4°$ model cell, a single k point at the Γ point was sufficient to properly describe the electronic structure of the model cell. The energy cutoff was set to 400 eV. The structures were relaxed until the residual forces were below 0.01 eV $Å^{-1}$. STM simulations were calculated using the Tersoff–Hamann[45] formalism. To supplement the XPS measurements, core level shifts of the oxygen 1s states were obtained in the final state approximation.[46] Dissociation barriers were calculated using the improved dimer method.[47,48]

3 Results

3.1 General aspects of water adsorption and desorption

3.1.1 TPD. Temperature programmed desorption (TPD) measurements form the backbone of the analysis of the behavior of water on ZrO_2/Pt_3Zr. Fig. 1(a) shows three distinct regions in the TPD spectrum for D_2O: two desorption peaks with maxima at 150 and 180 K, and a tail extending towards high temperatures. We also checked for simultaneous desorption of other species (m/z = 3, 4, 18, 19, and 28) and found no peaks apart from the D_2O cracking products. The desorption temperature of 150 K is typical for multilayer water.[9] When plotting this peak in a log(I) *vs.* 1/T plot, see Fig. 1(b), the ascending slope (dotted line) yields a desorption energy of 0.47 eV,[49,50] which is slightly lower than expected for multilayer D_2O ice (0.53 ± 0.02 eV; ref. 51). This may be due to the second-layer ice not having fully developed its crystalline order.

The TPD peak with the maximum at 180 K exhibits a first-order desorption behavior and reaches saturation at a coverage of approximately 1 ML (one D_2O molecule per Zr atom in the oxide); it is therefore the monolayer peak. The area of the monolayer peak does not stay perfectly constant during repeated TPD measurements, see the section on water-induced changes, below. On the high-temperature side of the monolayer peak, starting at approximately 190 K, the desorption rate decreases more slowly than expected for a first-order peak. The signal forms a long tail and vanishes below the detection limit at ≈540 K, see inset of Fig. 1(a) (comparison with D_2O TPD of other surfaces shows that the tail is not an instrumental artifact). The tail may consist of a multitude of peaks that cannot be

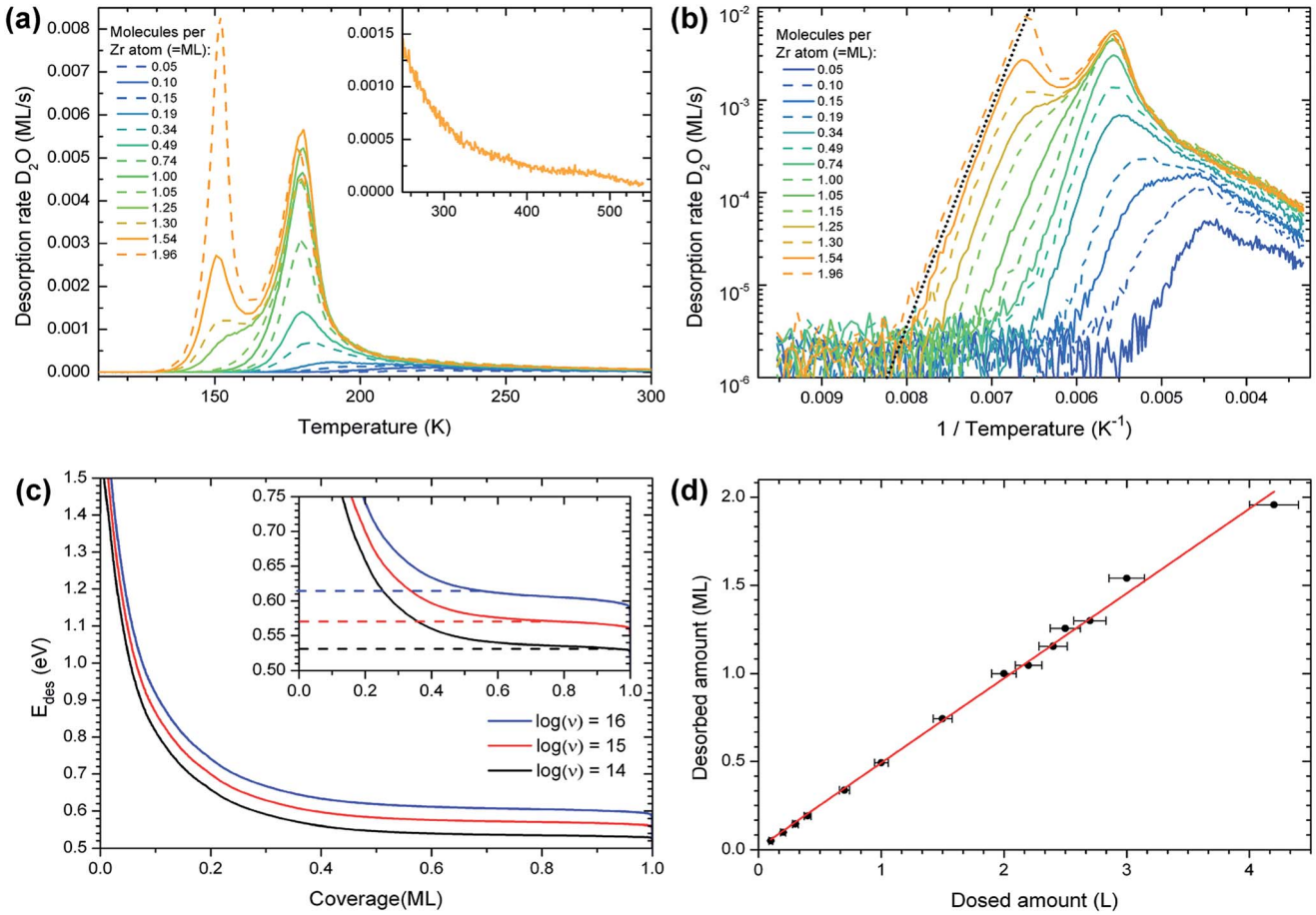

Fig. 1 TPD of D_2O on ZrO_2/Pt_3Zr (heating rate 1 K s^{-1}; no fresh sample preparation between spectra with different coverage). (a) The TPD spectra consist of three regions: the multilayer peak (150 K), the monolayer peak (180 K) and a high-temperature tail up to ≈540 K, see inset. (b) Logarithmic plot of the spectra in (a) *vs.* 1/*T*. The linear onset of the multilayer peak gives E_{des} = 0.47 eV. (c) Inversion analysis showing the desorption barrier E_{des} *vs.* coverage using $\nu = 10^{15\pm1}$ s^{-1}. In the 0.5–0.95 ML range, E_{des} is 0.57 ± 0.04 eV. (d) Amount of desorbed D_2O (calculated from the integrated TPD signal) as a function of gas dose. The TPD intensities were calibrated assuming a sticking coefficient of one, thus 1 Langmuir (*L*) = 10^{-6} torr s corresponds to 0.48 ML. The red line is a linear fit.

discerned from each other. The coverage in the tail corresponds to approximately 0.15 ML, while the rest of the monolayer makes up the peak at 180 K. When plotting the desorbed amount of water, taken from TPD, *vs.* the dosed amount, the intercept of a linear fit yields a dose of 0.01 ML (Fig. 1(d)). This shows, within the error of such an analysis, that no water was present on the surface before dosing.

The differential desorption energy E_{des} of water bound in the monolayer peak can be calculated using the inversion analysis method:[52,53] the Polanyi–Wigner formula (1), which describes the desorption rate $-d\theta/dt$ in dependence of coverage θ and temperature T,

$$\frac{d\theta}{dt} = -\nu(\theta)\theta^n \exp\left(\frac{-E_{des}(\theta)}{k_B T}\right) \quad (1)$$

is inverted under the assumptions of first-order desorption (n = 1), the prefactor ν being independent of θ, and a constant heating rate β:

$$E_{des}(\theta) = -k_B T \ln\left(-\frac{\beta}{\nu\theta}\frac{d\theta}{dT}\right) \quad (2)$$

where T is the temperature and t is the time. Eqn (2) is fully defined by the measured TPD data except for ν. To determine ν and E_{des}, we follow ref. 54 in using eqn (1) to simulate TPD spectra that consist mainly of the monolayer peak. In our case of D_2O on ZrO_2/Pt_3Zr, the best overlap between experimental and simulated curves is achieved at $\nu = 10^{15\pm1}$ s^{-1}. This is a typical value for water desorption.[8] Fig. 1(c) shows E_{des} as a function of θ, derived for an initial coverage of 1 ML. The desorption energy stays almost constant between 0.55 and 0.95 ML and amounts to 0.57 ± 0.04 eV, taking the error bars of ν into account.

At lower coverages (well inside the high-temperature tail), the results of the inversion analysis in Fig. 1(c) give adsorption energies of up to ≈1.5 eV. These energies should be treated with caution; here ν might vary considerably from the value determined for the monolayer peak (*e.g.* due to recombinative desorption or surface restructuring during desorption).

3.1.2 X-ray photoelectron spectroscopy. To determine whether (or to what extent) water adsorbs in molecular or dissociated form on the ZrO_2/Pt_3Zr surface, we have analyzed XPS O 1s data. When dosing 2 ML D_2O at 100 K, four different peaks are distinguished as originating from D_2O, OD, 3D ZrO_2

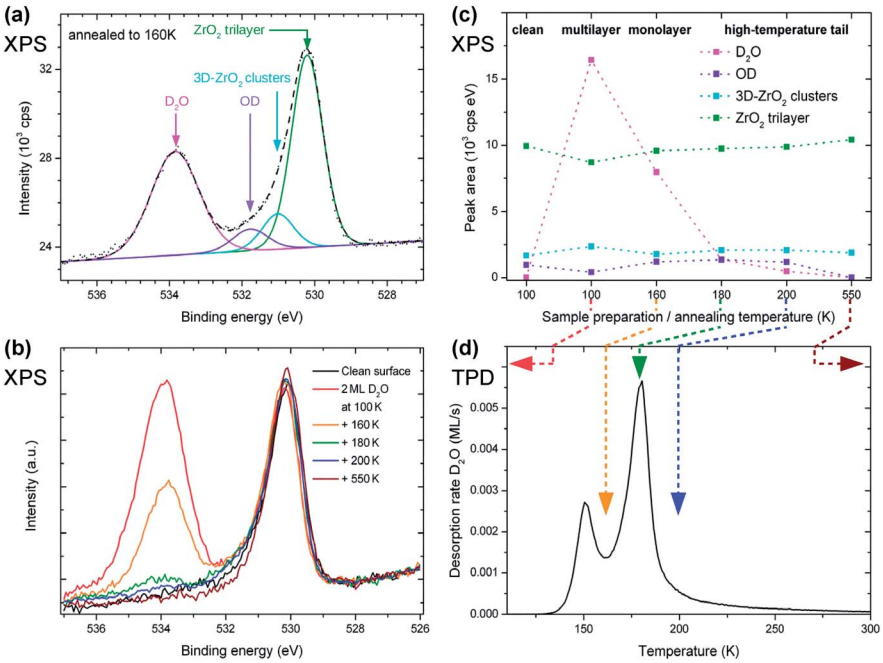

Fig. 2 XPS of D_2O on ZrO_2/Pt_3Zr. (a) O 1s region with 2 ML D_2O deposited at 100 K, then annealed to 160 K to remove the multilayer. (b) Comparison of spectra before and after D_2O adsorption, and after additional annealing steps. All XPS spectra were taken at 100 K. (c) Peak areas of the spectra in (b) for the peaks assigned to D_2O, OD, 3D ZrO_2 clusters, and the ZrO_2 trilayer. (d) TPD measurement (1.54 ML) for comparison with the XPS results in (b, c).

clusters, and the ZrO_2 trilayer, see Fig. 2(a). Fig. 2(b, c) shows the peak areas of these four different O 1s components after various flash-annealing steps. The peak at 530.1 eV originates from oxygen bound in the ZrO_2 trilayer and is very close to the reported value of 529.9 eV.[36] This peak does not change significantly with coverage or temperature, except for a slight decrease when the intensity is dampened by 2 ML D_2O. Within the accuracy of the fits, the peak attributed to 3D clusters also remains constant. (The trilayer and 3D ZrO_2 clusters have distinct O 1s and Zr 3d spectra;[36] the 3D cluster/trilayer ratio is consistent for O 1s and Zr 3d, which confirms the correctness of our peak fitting. An STM image of a 3D ZrO_2 cluster can be found in the ESI.†) The O 1s peak at 533.8 eV originates from non-dissociated D_2O.[6,55,56] When flash-annealing to 160 K, which is above the desorption temperature of the multilayer peak, yet below the desorption temperature of the monolayer peak, this peak decreases by roughly 50%, in agreement with only 1 ML remaining on the surface, see Fig. 2(c). When annealing to 180 K (maximum of the monolayer peak), the molecular D_2O peak decreases further and nearly vanishes at 200 K (beyond the monolayer peak). When annealing to 550 K, the spectrum decreases in the region 531–532 eV, *i.e.*, between the two main peaks. This region contains signals from oxygen in zirconia clusters (E_B = 531.0 eV)[36] and from hydroxy groups (E_B = 531.8 eV); a shift of 1.7 eV between the trilayer oxide peak and the hydroxy peak lies within the expected range.[6,55,57,58] Since zirconia clusters do not change when annealed at 550 K, the decrease stems solely from hydroxy groups. The TPD high-temperature tail is therefore due to dissociated water, which recombines before desorption. When comparing the O 1s signal from OD groups and from the ultra-thin film to XPS simulations using the SESSA program,[59] the amount of water present as hydroxy groups is estimated as 0.12 ML. A small hydroxy component appears also on the as-prepared oxide [labelled "clean" in Fig. 2(b, c)], possibly due to adsorption from the residual gas.

D_2O dissociation induced by X-ray beam damage was excluded by dosing 2 ML of D_2O at 100 K and annealing the sample directly to 200 K. This yielded exactly the same result as shown for 200 K in Fig. 2(b, c), showing that there is no dissociation while taking several X-ray photoelectron spectra.

3.1.3 Scanning tunneling microscopy. Fig. 3(a) shows 0.12 ± 0.04 ML of H_2O (dosed *via* back-filling of the chamber) on a freshly-prepared ZrO_2/Pt_3Zr surface at 100 K. This coverage corresponds to the high-temperature TPD tail. During measurements, the sample was held at 78 K. Both temperatures lie well below all desorption peaks of water, see above. Three different regions are present in the STM image: ordered, apparently uncovered and clustered areas. The water species in the ordered areas are stable during imaging; they typically appear as 80–100 pm high protrusions. The ordered areas mostly show the same periodicity as the ZrO_2 trilayer, *i.e.*, $(\sqrt{19} \times \sqrt{19})R23.4°$ with respect to the Pt layer below.[33] The clustered areas, presumably with a higher local coverage, appear fuzzy, indicating that the water molecules are moving under the influence of the tip. This suggests that one or two adsorption sites per unit cell are more stable than the others. Following the XPS measurements shown above, which show that the most stable adsorption sites are occupied by hydroxy groups, we attribute the ordered features to OH; this

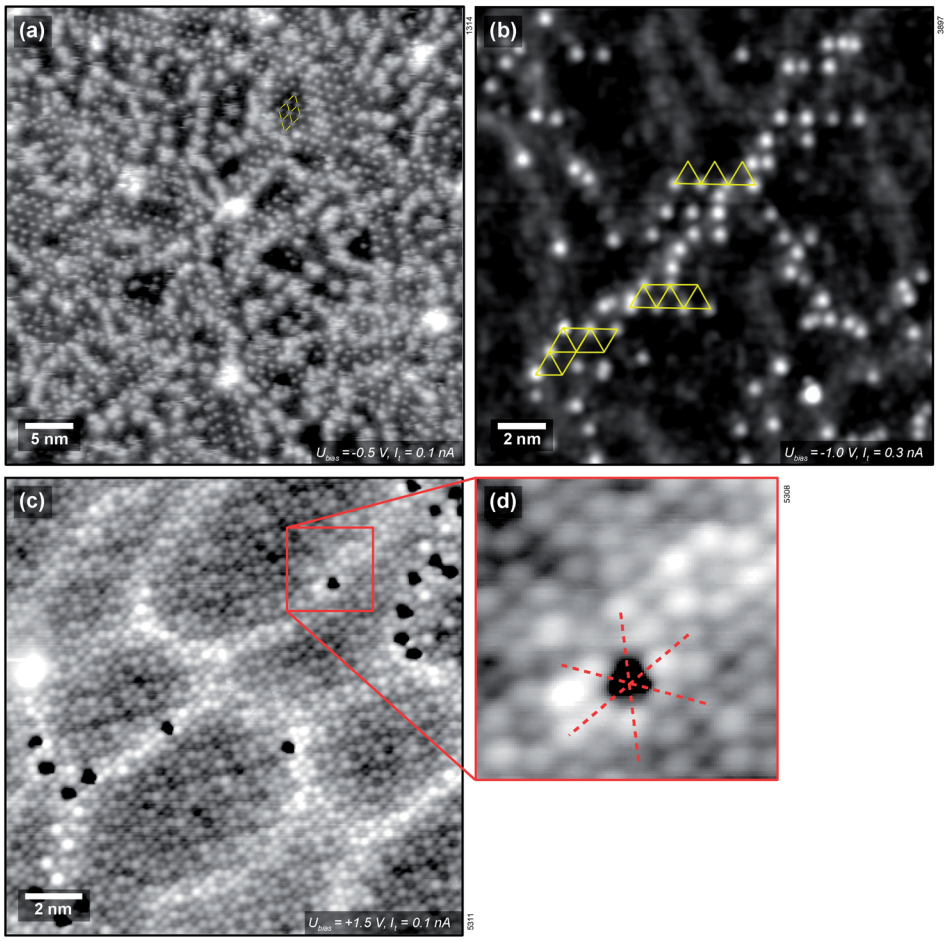

Fig. 3 STM of small H_2O coverages on ZrO_2/Pt_3Zr. (a) 0.12 ± 0.04 ML H_2O, dosed at 100 K, measured at 78 K. The surface consists of stable regions with water species arranged in the $(\sqrt{19} \times \sqrt{19})R23.4°$ structure (yellow dashes), regions with higher coverages and unstable imaging (fuzzy gray patches), and apparently uncovered regions of the ZrO_2 trilayer. (b) After dosing 15 L of H_2O at RT. Water-related species, namely O_wH, are found preferentially above subsurface dislocation lines (grey areas in the image). They locally show the $(\sqrt{19} \times \sqrt{19})R23.4°$ order (yellow). (c) The surface after dosing 30 L of H_2O at RT and storage in UHV for 8 hours. The image was obtained with a special tip that shows OH as depressions (black). Apart from the few hydroxy groups, the clean oxide surface can be seen with atomic resolution. The red lines in the zoom-in (d) indicate that the OH are on top of Zr atoms (protrusions in the image).

assignment is confirmed below. Dissociation of H_2O leads to two hydroxy groups, one (O_wH, also known as terminal OH) containing the oxygen atom of the water, and the other formed by a surface oxygen atom and the split-off proton (O_sH). These two OH groups should appear differently in STM. As we see only one type of distinct protrusion, we have to assume that STM shows the terminal OH, which is geometrically higher, while an adjacent O_sH is invisible due to its smaller apparent height. (This is in agreement with DFT, see below.) The coverage of one dissociated H_2O, *i.e.*, two OH groups, per $(\sqrt{19} \times \sqrt{19})R23.4°$ unit cell was used as the input for an XPS simulation using SESSA.[59] The result shows that this coverage accounts for ≈2/3 of the hydroxy groups seen in XPS.

When measuring H_2O on ZrO_2 at room temperature (well inside the high-temperature tail), only a low coverage of H_2O-related protrusions is found even after supplying large gas doses, see Fig. 3(b). This is in agreement with the TPD results. Again, the protrusions appear about 80–100 pm high. The $(\sqrt{19} \times \sqrt{19})R23.4°$ ordering can still be made out locally. Water adsorbs preferentially above the subsurface dislocation lines. As mentioned above, these stem from the misfit between the Zr-depleted Pt layer between the ZrO_2 trilayer and the Pt_3Zr substrate.[33] Furthermore, water adsorbs on top of rotational domain boundaries[34] of the oxide film (these are rather sparse; there is none in Fig. 3). Fig. 3(c) and (d) show single water species (hydroxy groups) adsorbed on a ZrO_2 trilayer, imaged with a special tip that lets these species appear as dark depressions. Assuming that the bright protrusions in the STM image (c, d) correspond to Zr as suggested for "normal" tips in ref. 33, the red lines indicate that the adsorption site of the water species is above a Zr atom. This is consistent with the site expected for the terminal O_wH.

3.2 Water-induced surface changes

While repeating D_2O TPD measurements on ZrO_2/Pt_3Zr, the monolayer peak changed over the course of several cycles, see

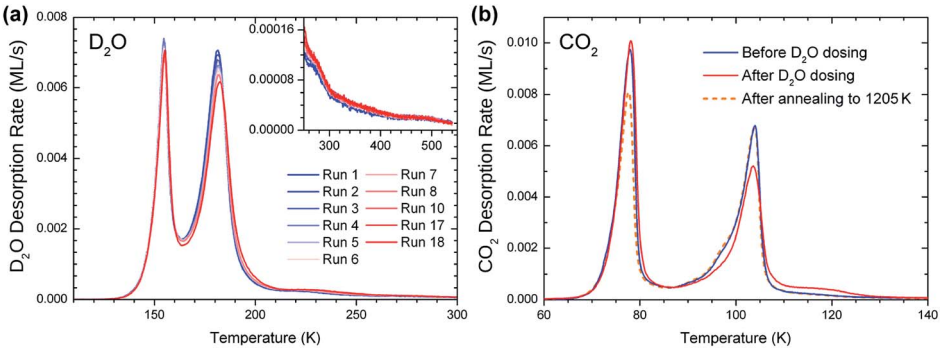

Fig. 4 Water-induced modification of the ZrO_2/Pt_3Zr trilayer. (a) Repeated D_2O TPD runs (heating rate 2 K s^{-1}) with a starting coverage of 2 ML each. The monolayer peak decreases while the high-temperature tail increases. (b) CO_2 TPD (initial dose ≈ 1 ML, heating rate 1 K s^{-1}) before (blue curve) and after (red) 18 D_2O TPD cycles. The increasing intensity in the 110–125 K range indicates an attractive interaction of CO_2 with the water-induced defect sites. Annealing to 1205 K restores the original state of the surface (orange, dashed).

Fig. 4(a). There, 18 successive TPD measurements were carried out, each starting with 2 ML D_2O dosed at 100 K and then ramped to 550 K (with one exception for the dose as noted below). The monolayer peak area decreases by 8% from the first to the 18th run, with the biggest decrease during the first cycles. At the same time, the amount of water desorbing above 185 K increases, such that the total amount of desorbed water remains constant (note that also the area of the multilayer peak stays constant within the experimental accuracy). Thus, the decreasing monolayer peak height is not due to an increasing amount of water remaining on the surface between TPD runs. These results rather show that, under the influence of repeated water adsorption/desorption cycles, adsorption sites with low E_{des} (T_{des} = 180 K) change to adsorption sites with higher E_{des}. Between the 8th and the 18th run, eight TPD cycles with 2 ML and one with 15 ML were interposed (not shown); dosing 15 ML affects the surface in the same way as 2 ML. The changing height of the 180 K peak is also visible in Fig. 1(a). (Note that the measurements in Fig. 1 were not done in the sequence of increasing or decreasing coverage, thus the 180 K peak heights at coverages above 1 ML seem to scatter randomly.) Such changes did not appear in multiple TPD cycles with CO_2, so they must be caused by the interaction of the surface with water, not by the heating/cooling cycles alone.

It was found that CO_2 TPD is a good indicator for the water-induced surface change, see Fig. 4(b). 1 ML of CO_2, corresponding to 1 CO_2 per surface Zr atom, was dosed (at 50 K) and desorbed by ramping the temperature to 300 K before the first and after the 18th D_2O TPD run. The CO_2 multilayer peak is at 78 K,[37] and the low-temperature (90–100 K) shoulder of the monolayer peak is attributed to compression of the CO_2 layer.[60,61] The monolayer peak (104 K) and the multilayer peak have roughly the same area, thus approximately one CO_2 molecule per two Zr atoms forms the monolayer. After the water adsorption/desorption cycles, the CO_2 monolayer peak area decreases and the high-temperature tail (105–130 K) increases by approximately 0.05 ML (≈10% of a CO_2 monolayer). When repeating the CO_2 TPD, there is no further change. The TPD behavior indicates that CO_2 binds more strongly to the newly-created sites. The moderate increase of the CO_2 adsorption energy points to electrostatic interaction between OH and the quadrupole moment of CO_2, rather than chemical bonding of CO_2, *e.g.* as bicarbonate (on TiO_2(110), the CO_2 TPD peak attributed to bicarbonate is at ≈213 K, ref. 62). We also note that the combined coverage of the monolayer (including the low-T shoulder) and tail slightly decreases after the D_2O cycles (by ≈5%). This reduction of the total amount of CO_2 bound in the first layer seems to be mainly related to less compression (weaker low-T shoulder). It is likely that the newly created sites with higher CO_2 and D_2O desorption energy pin the CO_2 layer, preventing the formation of a well-ordered compressed CO_2 layer.

We have also used STM to search for water-induced surface modifications. After one cycle of dosing 1.5 ± 0.3 ML water and annealing to 550 K, the surface appears as shown in Fig. 5(a) (STM at T = 78 K). The $(\sqrt{19} \times \sqrt{19})R23.4°$ superstructure of the ZrO_2 trilayer and the dislocation lines appear unchanged. A small number of water-induced features with an apparent height of 120–150 pm survives the 550 K annealing; their number increases with more adsorption/desorption cycles, and amounts to approx. 0.01 ML per adsorption cycle, fitting the results from the decrease of the ML peak mentioned above. Similar to the OH formed at room-temperature adsorption, these features preferentially bind to sites above the subsurface dislocation lines. After 5 cycles, see Fig. 5(b), some ordering of these water-induced features can be made out: in the Fourier transform of the positions of these species (inset of Fig. 5(b)), the strong outer spots (marked by red circles) indicate equivalent positions with respect to the 0.35 nm ZrO_2 lattice. There are also weaker spots corresponding to the $(\sqrt{19} \times \sqrt{19})R23.4°$ superstructure of the ZrO_2 trilayer on the oxide (blue circles), indicating that some sites in the superstructure are preferred over others. Based on the real-space images, there must be at least two such preferred positions. This behavior is similar to H_2O dosed at RT, see above. This observation can not be explained by H_2O or OH simply remaining on the surface bound to very stable adsorption sites without any surface change, as the density of water species (and therefore the density of sites) increases with the number of cycles. Likely, there is some modification (deformation) of the oxide film, leading to

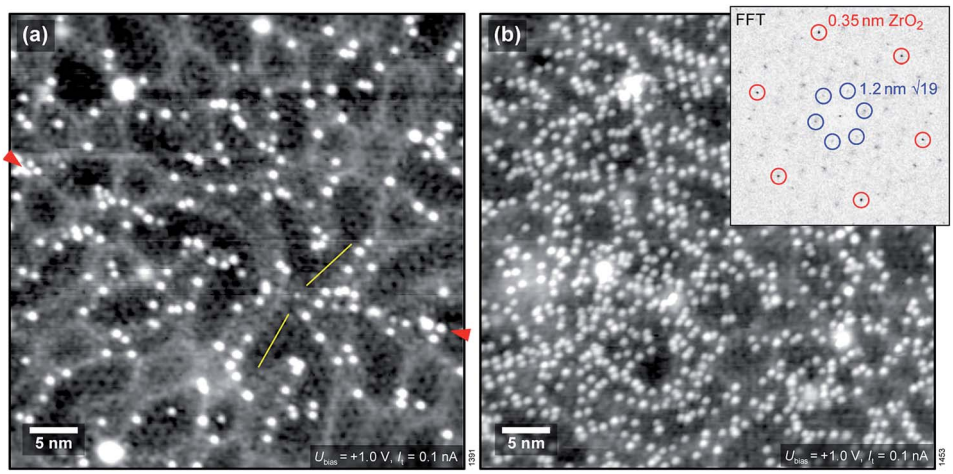

Fig. 5 Effect of H_2O adsorption/desorption cycles on the ZrO_2/Pt_3Zr trilayer seen by STM (T_{STM} = 78 K). (a) After one adsorption/desorption cycle. The water-induced bright species form preferentially on top of dislocation lines (gray bands) as well as at a rotational domain boundary [between the red arrows in the margins; the orientation of the $(\sqrt{19} \times \sqrt{19})R23.4^\circ$ unit cell on both sides of the DB is indicated by yellow lines]. (b) After five adsorption/desorption cycles, the coverage of the bright spots (O_wH) has increased by almost a factor of five. An FFT of the bright features (inset) indicates equivalent positions on the 0.35 nm ZrO_2 lattice and some influence by the $(\sqrt{19} \times \sqrt{19})R23.4^\circ$ superstructure.

stronger bonding to OH. Nevertheless, the oxide lattice remains largely intact as demonstrated by the sharp FFT spots.

3.3 Infrared measurements on monoclinic ZrO_2 powder samples

Water adsorption on a pre-sintered powder sample of monoclinic ZrO_2 was studied in isothermal (at room temperature) and isobaric experiments. For the isothermal measurements, water was dosed at pressures between 4×10^{-3} and 25 mbar (saturation vapor pressure). The infrared absorption spectra do not show any substantial discrete peaks but only a broad band of H-bonded species (Fig. 6(a)).[24] As this band does not change shape in the pressure range of interest, the amount of adsorbed water on the sample can be approximated by plotting the relative height/absorbance of this band *versus* the partial pressure. This approximation is justified by comparison with gravimetric experiments up to pressures where water condensation in capillaries appears, at about 80% relative humidity.[24] Since the absorption spectra show strong water gas-phase peaks at pressures above 10^{-2} mbar, the absorption was determined at wavenumbers near 3160 cm^{-1} (vertical line in Fig. 6(a)), where the signal intensity of gaseous water is zero (Q-branch of the first overtone of the δ rotational-vibrational mode[63]). An absolute calibration of coverage *vs.* absorption is not possible due to light scattering in the pressed powder.[64] Based on gravimetric data,[24] the FTIR signal at saturation water pressure (p_{H_2O} = 25 mbar) and room temperature corresponds to 20–30 molecules per nm^2, which is a factor of 2–3 above our previous monolayer definition of 1 H_2O per surface Zr.

Initial adsorption also induces a slight negative peak between 3700 and 3800 cm^{-1}, which we attribute to a small coverage of isolated species, becoming part of the H-bonded network at higher coverage. This frequency range indicates OH bound to one or two Zr atoms. Comparison of the shape of the band of H-bonded species between different pressures shows also an initial negative signal of comparable size superimposed on the broad band above 3650 cm^{-1}. Absorption in

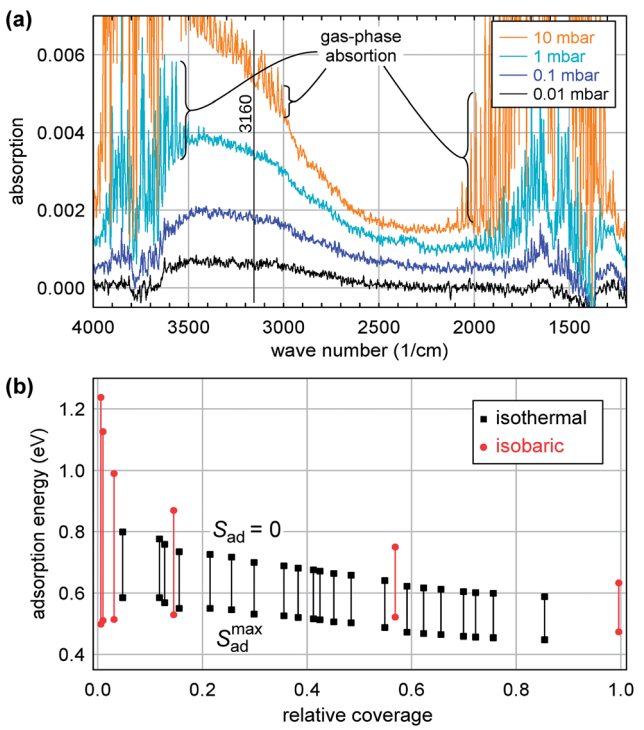

Fig. 6 Infrared absorption of H_2O on sintered monoclinic ZrO_2 powder. (a) Spectra at 298 K for selected partial pressures of H_2O. Spectra are shifted vertically for clarity, and a few regions of dense gas-phase absorption peaks are indicated. (b) Differential adsorption energies from the isobaric and isothermal measurements. The vertical lines span the results for the two extreme cases of zero (top) and maximum (ice-like, bottom) adsorbate entropy. Coverage values are normalized with respect to the value at p_{H_2O} = 25 mbar, which corresponds to 2–3 H_2O per surface Zr atom.

this frequency range is frequently observed on monoclinic ZrO_2 and attributed to threefold-coordinated OH.[65,66]

In addition, an isobaric experiment was performed. This experiment was performed in flowing mode by passing helium through a water vapor saturator at room temperature (p_{H_2O} = 25 mbar) and monitoring the infrared absorption as a function of temperature. These data are less accurate than the isothermal ones due to various instrumental factors as well as the increasing appearance of ZrO_2 lattice vibrational overtones in the spectra; nevertheless the results are valuable for the analysis (see below).

For determination of adsorption enthalpies, we make use of the fact that the chemical potentials μ_{ad} of the adsorbed and μ_g of the gas phase must be equal in equilibrium:

$$\mu_g = H_g - TS_g = \mu_{ad} = -E_{ad} - TS_{ad} \quad (3)$$

where the enthalpy H_g and entropy S_g per molecule in the gas phase is calculated from tabulated data (assuming an ideal gas).[67] E_{ad} is the adsorption energy per atom. We define E_{ad} as a positive number for stable adsorption sites, as above, thus the minus sign. The volume of the adsorbed H_2O can be neglected, *i.e.*, its energy and enthalpy are assumed to be equal. For calculating the adsorption energy, E_{ad}, which can be directly compared to the DFT and TPD results above, we need to know S_{ad}, the entropy per molecule in the adsorbed state. S_{ad} has a configurational contribution due to the multiple adsorption sites available below saturation, with an upper limit of $-k_B \ln \theta$ (we use the saturation coverage for $\theta = 1$, but changing this to, *e.g.*, 1 H_2O per surface Zr atom has only a very minor influence on the calculated E_{ad}). This upper limit is reached if all sites are equal and there is no interaction between adsorbates. The other contribution to S_{ad} comes from the adsorbate's vibrational and orientational degrees of freedom. For submonolayer coverages, the substrate provides a corrugated potential-energy landscape acting as a template for the adsorbate preventing a liquid layer, see the DFT results below. Therefore, we may safely assume that the adsorbed H_2O is bound and confined at least as strongly as in ice. Thus, we take the entropy of ice, extrapolated to temperatures above 0 °C as an upper limit of its entropy:

$$S_{ad}^{max} = -k_B \ln \theta + S_{ice}^{extrap}(T) \quad (4)$$

Since $S_{ice}^{extrap}(T)$ is almost linear in temperature between 150 and 273 K,[68] we use a linear fit, which yields $S_{ice}^{extrap}/(\text{eV K}^{-1}) = (3.69 \times 10^{-5} + 1.42 \times 10^{-6}\ T/\text{K})$. (We have also tried using the entropy of liquid H_2O here. This would result in unphysical adsorption energies below the vaporization energy of H_2O, however, supporting our choice of ice for estimating the entropy.)

Fig. 6(b) shows the result of this calculation for both the isothermal (T = 298 K) and the isobaric (298–573 K) experiments. The bars span the range between the two limits for the entropy, zero and S_{ad}^{max} (4). For low coverage, these two experiments correspond to substantially different temperatures, thus a comparison between them can be used to estimate the entropy. As expected, the agreement is better for the upper limit of the entropy, *i.e.*, the configurational entropy of the adsorbed layer cannot be neglected and the vibrational and orientational entropies are similar to ice. Nevertheless, we think that the actual entropy must be slightly less than the upper limit since the assumption of S_{ad}^{max} yields a reversal of the slope of the isobaric adsorption energies at low coverages, which we consider unrealistic. Therefore, our best guess is an adsorption energy of ≈0.65 eV at low coverages, decreasing to values close to the binding energy in ice at 1 ML. It should be noted that similar values of the adsorption energies could be also obtained from a Langmuir adsorption isotherm (≈0.62 eV over a large range of coverages, when assuming a constant prefactor of 10^{15} s^{-1}). This method was already used for adsorption studies on zirconia.[24,69] Compared with the present approach, the disadvantage of the Langmuir model is that the entropies of the gas and the adsorbed phase are hidden in the prefactor and effects such as temperature-dependent rotational and vibrational gas-phase entropies or coverage-dependent configurational entropies of the adsorbed phase will necessarily lead to a non-constant prefactor.

As mentioned, the adsorption energies in Fig. 6(b) are based on the broad absorption band and do not include the isolated species giving rise to the negative adsorption peak discussed above. Thus, one should expect the zero of the coverage scale of Fig. 6(b) a bit further to the left than shown, with higher adsorption energies at these very low coverages.

3.4 DFT calculations

The experiments by Antlanger *et al.*[33] have shown that the ultrathin ZrO_2 film forms a commensurate $(\sqrt{19} \times \sqrt{19})R23.4°$ supercell with respect to the Pt lattice, which forms the interface to the $Pt_3Zr(0001)$ substrate below. Each unit cell contains 12 formula units of ZrO_2, which results in an average ZrO_2 in-plane lattice constant of 350 pm. Since accounting for the alloy as the substrate would require a very large unit cell (>500 atoms), a pure 5-layer Pt(111) slab served as the supporting structure of the ZrO_2 film in our calculations (d_{Pt-Pt} = 277.8 pm; bottom two Pt layers fixed). The viability of such a model has been shown by Meinel *et al.*[28] and for modeling the adsorption of metal adatoms by Choi *et al.*[34]

3.4.1 The ZrO_2 film. Structural optimization using a simulated-annealing approach leads to a heavily distorted ZrO_2 film, shown in Fig. 7(a). With the occurrence of twofold coordinated O atoms at the surface, this structure is similar to the one found by Puigdollers *et al.*[70] using a PBE+U functional, and very similar to our previous result[34] (which is only a local energy minimum according to our present study). Probably due to the flat potential-energy landscape with a large number of local minima, also the present structure does not perfectly represent the experimental one in all details. *E.g.*, Fig. 3(c) suggests a higher symmetry than the DFT model in Fig. 7a. Nevertheless, the main structural elements should be represented well enough to capture the key features for the interaction with the water molecules. The interlayer distances between the mean layer heights, d_{O-Zr}, d_{Zr-O}, and d_{O-Pt}, are 93, 72, and 223 pm, respectively, and all oxide layers are strongly buckled (125, 116, and 96 pm peak–peak for the upper O, Zr, and lower O layer). The group of six high-lying Zr atoms,

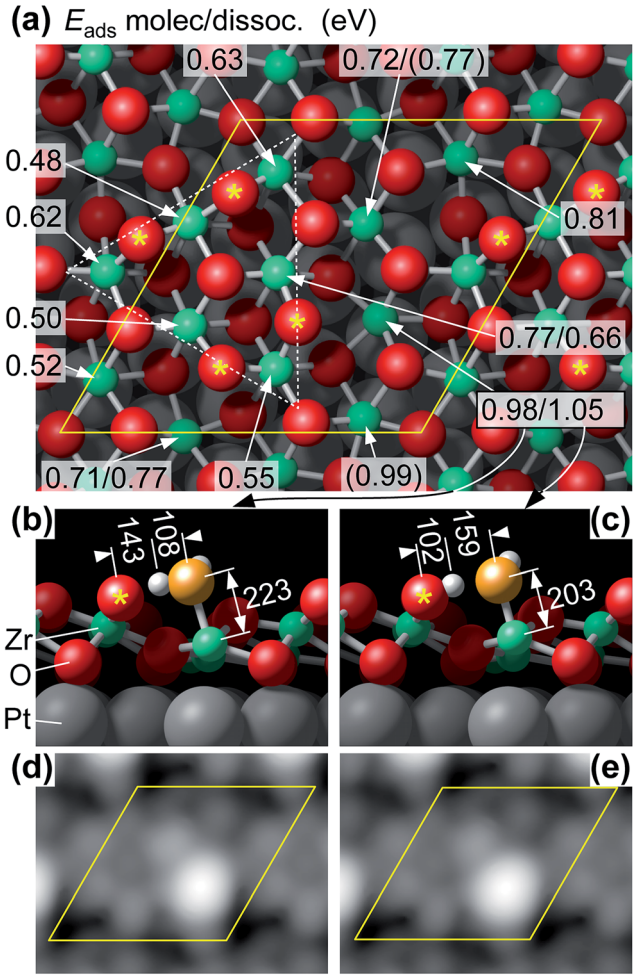

Fig. 7 H_2O adsorption on a trilayer ZrO_2 film in DFT. (a) Top view of the fully-relaxed $(\sqrt{19} \times \sqrt{19})R23.4°$ model cell including adsorption energies (in eV) at water adsorption sites. For selected sites, energies of dissociative adsorption are given after the slash. Values in parentheses indicate that the ZrO_2 film had moved and changed upon adsorption, resulting in a site of different character. The yellow rhombus indicates the unit cell, and the dashed triangle shows the group of six Zr atoms higher than the others. Twofold-coordinated oxygen atoms are marked by yellow asterisks. Side view of (b) molecularly bound and (c) dissociated water at the site marked "0.98/1.05", with bond lengths in pm. These two configurations are indistinguishable in the STM simulations (d, e).

marked with a dashed white triangle in Fig. 7(a), have contracted Zr–Zr distances of 323 to 347 pm. They are separated by low-lying Zr ("valleys") with Zr–Zr distances up to 389 pm. In the high Zr triangles, the interaction between the ultra-thin oxide film and the Pt(111) substrate is dominated by the lower oxygen atoms of the trilayer, while in the valleys the Zr atoms bind strongly to the Pt surface atoms. This distortion breaks four Zr–O bonds at the surface, leading to a twofold coordination of some of the oxygen atoms at the borders of the high triangles.

3.4.2 Adsorption of H_2O on the ultrathin film. To screen a large number of adsorption sites, 36 starting configurations with the H_2O molecule positioned in a 6×6 grid with respect to the surface unit cell were tested. After the relaxation, the H_2O molecule had always moved to one of the twelve Zr surface atoms. The adsorbed H_2O molecule does not dissociate spontaneously in any of these twelve sites. Due to the distortions of the ZrO_2 film, these H_2O adsorption sites have substantially different local geometries, which leads to a wide range of calculated adsorption energies, from 0.48 to 0.99 eV (see Fig. 7(a)). For isolated H_2O molecules, adsorption at the laterally compressed "high" Zr atoms is mostly on the weaker side, (0.48–0.77 eV), also reflected by comparably long Zr–O_w distances around 236 pm. Adsorption is stronger at valley sites (0.62–0.99 eV), where the ultra-thin ZrO_2 film is stretched, making the Zr atoms more reactive and accessible. The strongest adsorption is found where the H_2O molecule can form a hydrogen bond to an undercoordinated (twofold) oxygen atom at the border of a "high" Zr group (marked with energy 0.98 in Fig. 7(a); the site "(0.99)" is equivalent, after shifting of the film). A side view of this position with the O–H bond lengths is shown in Fig. 7(b). Due to the short H bond, dissociation *via* proton hopping is easy (67 meV barrier in DFT). At this site and one other (marked 0.71/0.77 in Fig. 7(a); not counting sites where the oxide film gets substantially shifted), dissociation is slightly more favored than molecular adsorption, see Fig. 7(c).

STM simulations show essentially identical images for molecular and dissociated water, see Fig. 7(d, e); the maxima are caused by the adsorbed water molecule and the terminal O_wH, respectively. This is not surprising as the difference between the two structures is only a small displacement ($\approx$40 pm) of the lower of the two protons, and an even smaller displacement of the O_w ($\approx$14 pm).

Upon adsorption of a full monolayer, *i.e.*, one H_2O molecule per Zr atom, the mean adsorption energy decreases to a value of 0.68 eV. It should be noted that the calculated ground state is not formed when each Zr atom is covered by one H_2O molecule. Instead, the H_2O molecules cluster above the "high" Zr atoms, connected by H_2O chains across the valleys. However, our calculations show that the optB86 functional overestimates the formation energy of hexagonal bulk ice Ih with a calculated value of 0.74 eV compared to the experimental value ($\approx$0.58 eV, ref. 71). This overestimation of the binding between H_2O molecules will artificially increase the tendency for the formation of water clusters. Nevertheless, our calculations show that the adsorption energy in the high-coverage limit is close to the binding energy of multilayer ice.

We have also calculated the core level binding energies of the O 1s states to confirm the identification of the different species by XPS. In the final-state approximation, taking the average binding energy of the O 1s states of the ZrO_2 film as a reference, the core levels shift towards higher binding energies by 1.1 eV and 3.55 eV for the dissociated and molecular adsorbates, respectively. This agrees well with the respective experimental values of 1.7 eV and 3.7 eV. Only small changes of the core level shift of about 0.1 eV are predicted for the different adsorption sites.

Finally, we have performed selected calculations for two ZrO_2 trilayers using the same lateral cell size as for one trilayer. These results should be seen with caution, however, as the film is strained (thicker films should approach the bulk lattice

constant, which is ≈3% larger), and due to the large number of local energy minima. Nevertheless, as a general trend it appears that adsorption energies increase with thickness, in agreement to DFT calculations in the literature for monoclinic bulk $ZrO_2(\bar{1}11)$ showing adsorption energies up to ≈1.2 eV.[65,72]

4 Discussion

Combining the data from literature and our results, a simple picture emerges for H_2O at all pure zirconia surfaces: at low coverages, H_2O is strongly bound at a few sites, with adsorption energies up to 1.5 eV or more. When these sites are saturated, experimental adsorption energies are around 0.6 eV. The TPD value of 0.45 eV for 7 ML films on Pt(111)[31] is an exception, probably due to the simplistic assumption of the prefactor being 10^{13} s^{-1}: the TPD peak in ref. 31 is 20 K above the multilayer peak, comparable to ours. Strongly bound water seems to be mostly dissociated; the weakly bound H_2O is in molecular form at least at low temperatures on our ultrathin films. Both our DFT results for the ultrathin films and DFT calculations for H_2O on monoclinic ZrO_2 from the literature[65,72] predict dissociative adsorption at (some or all) twofold-oxygen sites, otherwise mostly molecular adsorption, in many cases forming H-bonded structures already at low coverage. This also nicely fits our XPS data as well as FTIR, where the absence of sharp peaks in FTIR spectroscopy (except for the negative peak from the initial coverage) can be explained only by ensembles of H-bonded species on the monoclinic powder sample. With the H_2O molecules on top of the Zr atoms, and in-plane Zr–Zr distances of ≈330–400 pm, the H_2O–H_2O spacing is too large for a two-dimensional ice-like network of H-bonded species (O–O spacings in ice are 275 pm). Thus, at low coverages, we should not expect extended areas of a 2D water film but only ensembles of very few of H-bonded species.

The DFT energies for water on the ultrathin film agree reasonably well with experiment, especially when considering the overestimation of H bonding with the current functional. For bulk monoclinic ZrO_2 (m-ZrO_2), the experimental adsorption energies at low coverage are very high (≳2 eV;[21,22] our FTIR study does not give any value for the adsorption energy of the species leading to the negative peak). These values are even above DFT-calculated values for flat surfaces,[65,72] probably related to defects. However, at high coverages, all experiments (including our FTIR) indicate values of ≈0.6 eV, while DFT predicts strong H_2O adsorption on bulk m-ZrO_2, with typical adsorption energies in the 0.8–1.2 eV range.[65,72] Our own test calculations for a few H_2O/m-ZrO_2 configurations show similar results. To some degree, the problem may be blamed on overestimation of the strength of H bonds (as mentioned previously); this mainly affects the energies at high coverages.

The density of sites with high adsorption energy ("defect sites") depends strongly on the type of samples used. Astonishingly, it is rather high for 7 ML ZrO_2/Pt(111) films,[31] when compared with the ≈15% TPD tail in our ultrathin films. For our powder samples, it may come as a surprise that almost no strongly-bound H_2O is detected. To some degree, this may be an experimental artifact: as the reference spectrum was acquired after high-temperature annealing; very strongly bound hydroxy groups or H_2O readsorbed while cooling in vacuum would be included in the reference spectrum and go undetected. The density of these species should be small, however, as indicated by the small negative peak occurring when the preadsorbed H_2O joins the H-bonded adsorbates. The low density of defect sites in our powder samples may be due to the extensive high-temperature annealing (1 h at 1273 K in pure O_2), which is also responsible for the low specific surface area.

So what are these "defects" with high adsorption energy? We start this discussion by analyzing the DFT results for the ultrathin film. DFT indicates that this film is strongly distorted. Considering the sharp TPD peak (Fig. 1) and the large variation of the DFT adsorption energies (Fig. 7), we believe that DFT overestimates the heterogeneity of the surface (and, related, the distortions). Nevertheless, DFT tells us that the film structure is rather unstable, prone to distortions, and breaking of Zr–O bonds that lead to twofold-oxygen sites. We consider it likely that this kind of instability is responsible for the changes induced by multiple adsorption/desorption cycles, which create additional defect sites. DFT reveals a complex potential-energy landscape of the uncovered ultrathin oxide, but also the variety of bulk structures of similar energy[73] can be seen as the root of this instability. The STM results indicate stronger water bonding at one or two of the 12 Zr sites per $(\sqrt{19} \times \sqrt{19})R23.4°$ unit cell, in agreement with the ≈12% defect sites. At room temperature, water is stable at such sites only above subsurface dislocations of the substrate, again showing that a minor disturbance (slight distortions of the substrate) significantly influences the ultrathin oxide. The calculated $E_{ads} = 1.05$ eV for the most stable site in the supercell indicates that dissociated water should be barely stable for extended times at room temperature, which nicely fits these STM results, so these defect sites are probably similar to Fig. 7(c).

DFT suggests that twofold oxygen is the site of H_2O dissociation and provides an anchor[65,72] for further H_2O by H bonding. Given that the most stable surfaces[74] of monoclinic ZrO_2 exhibit at least 1/4 twofold oxygen atoms in the surface, and our FTIR study of well-annealed m-ZrO_2 suggests a low defect concentration, it is unlikely that a twofold oxygen is sufficient to qualify as a defect site. Our DFT results (Fig. 7(a)) show substantially different adsorption energies adjacent to twofold-oxygen sites, suggesting that the details of the geometry at a twofold oxygen and the Zr atom where H_2O adsorbs (and dissociates) strongly influences the bonding strength. This implies that not all twofold oxygens provide strong bonding to H_2O. On the other hand, DFT predicts much stronger H_2O adsorption on m-ZrO_2 than found in many experiments (including ours), which would indicate that the twofold oxygen atoms on m-ZrO_2 are not present or somehow blocked in reality.

Of course, there might be also other defects. We can probably exclude the most common defect[75] of oxide surface science, oxygen vacancies: for the tetragonal ZrO_2(101) surface (equivalent to {111}-type surfaces of cubic or monoclinic ZrO_2), the formation energy of oxygen vacancies at the surface is higher than in the bulk.[70] Also for m-$ZrO_2(\bar{1}11)$, our calculations yield a high oxygen vacancy formation energy of 7.1 eV. This means

that the concentration of oxygen vacancies at these surfaces will be negligible. Calculations for the ultrathin ZrO_2 trilayer suggest much lower oxygen vacancy formation energies (2.23 eV).[70] Oxygen vacancies, if present, should be easily filled by H_2O, and the desorption barrier at these sites should be high. Our TPD + XPS experiments exclude a significant amount of such species, however. Therefore, we believe that the concentration of oxygen vacancies at the surface of the trilayer ZrO_2 film is also negligible. Concerning minority sites, we should also consider that our ultrathin-film model system contains 3D ZrO_2 clusters.[36] The XPS signal from the clusters (Fig. 2(a)) is about 18% of that from the ultrathin film. Our STM images indicate that the average cluster height is at least four trilayers. With these values, an XPS simulation[59] indicates that clusters account for less than 7% of the surface area. This area is not enough to have a large impact on our XPS and TPD results; *e.g.*, a picture where all strongly bound or dissociated water is adsorbed on the 3D clusters would be inconsistent with the area fraction of the clusters.

Let us now compare H_2O adsorption on ZrO_2 to structurally similar oxygen-terminated surfaces. The TPD peak temperature of H_2O on the ultra-thin $ZrO_2/Pt_3Zr(0001)$ at 180 K is higher than on other oxygen-terminated oxides such as ultrathin alumina (164–168 K)[76,77] or a 2 ML-thick FeO film (H_2O: 166 K, D_2O: 169 K).[78] At least for the case of alumina, the top O–Al interlayer spacing (40 pm)[79] is less than in the present case, so the stronger bonding of H_2O on ZrO_2 must be explained by the large in-plane O–O spacing ($\approx$350 pm) on ZrO_2; this makes the metal cations more accessible than on most other oxygen-terminated oxides, where O–O distances are around 300 pm. Strong adsorption requires that the metal cations are easily accessible; for O-terminated surfaces this means large O–O distances. Examples of structures with O–O distances similar to ZrO_2 are $CeO_2(111)$[80] with the main TPD peak at 200 K and $In_2O_3(111)$ with H_2O adsorption energies of 1.2 eV (TPD peak well above room temperature).[57]

Finally, how good a model system is the ultrathin ZrO_2 film for "real-world" ZrO_2 surfaces? The ultrathin film is based on a trilayer of cubic $ZrO_2(111)$ with additional distortions and some twofold-coordinated O atoms at the surface. Thus, geometrically it is similar to the two energetically most favorable monoclinic ZrO_2 surfaces, $(\bar{1}11)$ and (111).[74] When comparing with ZrO_2 powder, nanocrystalline material will also exhibit a substantial number of edge and corner sites (more than the step sites in our model system), but for the high-temperature annealed material used for our FTIR study we do not expect enough of these sites to play an important role. As is generally true for ultrathin oxide films on metal substrates, the main restriction as a model system applies if adsorption involves charge transfer. In such a case, one should expect stronger bonding on the ultra-thin film than on thick films or bulk materials, where charge transfer is difficult or impossible.[34,81,82] For adsorption of H_2O, in molecular or dissociated form, there is no net charge transfer, so the fidelity of the film as a model system is probably limited by differences in geometry between the film and bulk structures. Unfortunately, the current DFT models do not agree well enough with experimental data for an exact comparison. Nevertheless, the good agreement of experimental H_2O adsorption energies is encouraging.

5 Conclusion

We have investigated the adsorption and desorption of water on a trilayer of ZrO_2 grown by oxidation of a $Pt_3Zr(0001)$ single crystal. With a combined TPD, XPS, and STM approach, we could show that $\approx$88% of the water molecules in the first monolayer adsorb molecularly, with an adsorption energy of $E_{des} = 0.57 \pm 0.04$ eV. This agrees well with DFT, which finds dissociative adsorption in only a few sites, with the proton accepted by twofold coordinated oxygen. Experiments also showed that the adsorption energies of dissociated water vary over a wide range, depending on local details of the structure (*e.g.* substrate dislocations below) and pretreatment (increasing number of "defect" sites after multiple adsorption-desorption cycles). FT-IR measurements on ZrO_2 powder showed similar adsorption energies as our UHV TPD study, indicating that the ultrathin (trilayer) ZrO_2 film is a valid model system for water adsorption on well-annealed real-world ZrO_2 surfaces.

Conflicts of interest

There are no conflicts to declare.

Acknowledgements

We would like to thank Günther Rupprechter and Christoph Rameshan for lending a $Pt_3Zr(0001)$ sample to us. This work was supported by the Austrian Science Fund FWF (SFB program F45 Functional Oxide Surfaces and Interfaces "FOXSI") and the Vienna Scientific Cluster (VSC). J. H. and G. S. P. acknowledge support by FWF Start grant Y847-N20.

Notes and references

1 E. S. Hecht, G. K. Gupta, H. Zhu, A. M. Dean, R. J. Kee, L. Maier and O. Deutschmann, Methane reforming kinetics within a Ni–YSZ SOFC anode support, *Appl. Catal., A*, 2005, **295**, 40–51, DOI: 10.1016/j.apcata.2005.08.003.

2 K. Tanabe, Surface and catalytic properties of ZrO_2, *Mater. Chem. Phys.*, 1985, **13**, 347–364, DOI: 10.1016/0254-0584(85)90064-1.

3 Y. Liu, J. Parisi, X. Sun and Y. Lei, Solid-state gas sensors for high temperature applications – a review, *J. Mater. Chem. A*, 2014, **2**, 9919–9943, DOI: 10.1039/C3TA15008A.

4 M. Hisbergues, S. Vendeville and P. Vendeville, Zirconia: Established facts and perspectives for a biomaterial in dental implantology, *J. Biomed. Mater. Res., Part B*, 2009, **88**, 519–529, DOI: 10.1002/jbm.b.31147.

5 M. A. Henderson, The interaction of water with solid surfaces: fundamental aspects revisited, *Surf. Sci. Rep.*, 2002, **46**, 1–308, DOI: 10.1016/S0167-5729(01)00020-6.

6 P. A. Thiel and T. E. Madey, The interaction of water with solid surfaces: Fundamental aspects, *Surf. Sci. Rep.*, 1987, **7**, 211–385, DOI: 16/0167-5729(87)90001-X.

7 R. Mu, Z.-j. Zhao, Z. Dohnálek and J. Gong, Structural motifs of water on metal oxide surfaces, *Chem. Soc. Rev.*, 2017, **46**, 1785–1806, DOI: 10.1039/C6CS00864J.

8 C. T. Campbell and J. R. V. Sellers, Enthalpies and entropies of adsorption on well-defined oxide surfaces: Experimental measurements, *Chem. Rev.*, 2013, **113**, 4106–4135, DOI: 10.1021/cr300329s.

9 G. S. Herman, Z. Dohnálek, N. Ruzycki and U. Diebold, Experimental investigation of the interaction of water and methanol with anatase–TiO_2(101), *J. Phys. Chem. B*, 2003, **107**, 2788–2795, DOI: 10.1021/jp0275544.

10 M. J. Stirniman, C. Huang, R. S. Smith, S. A. Joyce and B. D. Kay, The adsorption and desorption of water on single crystal MgO(100): The role of surface defects, *J. Chem. Phys.*, 1996, **105**, 1295–1298, DOI: 10.1063/1.471993.

11 Z. Zhang, O. Bondarchuk, B. D. Kay, J. M. White and Z. Dohnálek, Imaging water dissociation on TiO_2(110): Evidence for inequivalent geminate OH groups, *J. Phys. Chem. B*, 2006, **110**, 21840–21845, DOI: 10.1021/jp063619h.

12 R. Schaub, P. Thostrup, N. Lopez, E. Lægsgaard, I. Stensgaard, J. K. Nørskov and F. Besenbacher, Oxygen vacancies as active sites for water dissociation on rutile TiO_2(110), *Phys. Rev. Lett.*, 2001, **87**, 266104, DOI: 10.1103/PhysRevLett.87.266104.

13 M. A. Henderson, Structural sensitivity in the dissociation of water on TiO_2 single-crystal surfaces, *Langmuir*, 1996, **12**, 5093–5098, DOI: 10.1021/la960360t.

14 M. A. Henderson and S. A. Chambers, HREELS, TPD and XPS study of the interaction of water with the α-Cr_2O_3(001) surface, *Surf. Sci.*, 2000, **449**, 135–150, DOI: 10.1016/S0039-6028(99)01246-7.

15 M. A. Henderson, S. A. Joyce and J. R. Rustad, Interaction of water with the (1×1) and (2×1) surfaces of α-Fe_2O_3(012), *Surf. Sci.*, 1998, **417**, 66–81, DOI: 10.1016/S0039-6028(98)00662-1.

16 X. L. Hu, J. Carrasco, J. Klimeš and A. Michaelides, Trends in water monomer adsorption and dissociation on flat insulating surfaces, *Phys. Chem. Chem. Phys.*, 2011, **13**, 12447, DOI: 10.1039/c1cp20846b.

17 D. Halwidl, W. Mayr-Schmölzer, D. Fobes, J. Peng, Z. Mao, M. Schmid, F. Mittendorfer, J. Redinger and U. Diebold, Ordered hydroxyls on $Ca_3Ru_2O_7$(001), *Nat. Commun.*, 2017, **8**, 23, DOI: 10.1038/s41467-017-00066-w.

18 A. Lobo and H. Conrad, Interaction of H_2O with the RuO_2(110) surface studied by HREELS and TDS, *Surf. Sci.*, 2003, **523**, 279–286, DOI: 10.1016/S0039-6028(02)02459-7.

19 H. H. Kan, R. J. Colmyer, A. Asthagiri and J. F. Weaver, Adsorption of water on a PdO(101) thin film: Evidence of an adsorbed HO–H_2O complex, *J. Phys. Chem. C*, 2009, **113**, 1495–1506, DOI: 10.1021/jp808008k.

20 M. Meier, J. Hulva, Z. Jakub, J. Pavelec, M. Setvin, R. Bliem, M. Schmid, U. Diebold, C. Franchini and G. S. Parkinson, Water agglomerates on Fe_3O_4(001), *Proc. Natl. Acad. Sci. U. S. A.*, 2018, 201801661, DOI: 10.1073/pnas.1801661115.

21 S. V. Ushakov and A. Navrotsky, Direct measurements of water adsorption enthalpy on hafnia and zirconia, *Appl. Phys. Lett.*, 2005, **87**, 164103, DOI: 10.1063/1.2108113.

22 A. V. Radha, O. Bomati-Miguel, S. V. Ushakov, A. Navrotsky and P. Tartaj, Surface enthalpy, enthalpy of water adsorption, and phase stability in nanocrystalline monoclinic zirconia, *J. Am. Ceram. Soc.*, 2009, **92**, 133–140, DOI: 10.1111/j.1551-2916.2008.02796.x.

23 T. M. Orlando, A. B. Aleksandrov and J. Herring, Electron-stimulated desorption of H^+, H_2^+, OH^+, and $H^+(H_2O)_n$ from water-covered zirconia surfaces, *J. Phys. Chem. B*, 2003, **107**, 9370–9376, DOI: 10.1021/jp030117k.

24 E.-M. Köck, M. Kogler, B. Klötzer, M. F. Noisternig and S. Penner, Structural and electrochemical properties of physisorbed and chemisorbed water layers on the ceramic oxides Y_2O_3, YSZ, and ZrO_2, *ACS Appl. Mater. Interfaces*, 2016, **8**, 16428–16443, DOI: 10.1021/acsami.6b03566.

25 M. Kogler, E.-M. Köck, T. Bielz, K. Pfaller, B. Klötzer, D. Schmidmair, L. Perfler and S. Penner, Hydrogen surface reactions and adsorption studied on Y_2O_3, YSZ, and ZrO_2, *J. Phys. Chem. C*, 2014, **118**, 8435–8444, DOI: 10.1021/jp5008472.

26 E.-M. Köck, M. Kogler, T. Bielz, B. Klötzer and S. Penner, In situ FT-IR spectroscopic study of CO_2 and CO adsorption on Y_2O_3, ZrO_2, and yttria-stabilized ZrO_2, *J. Phys. Chem. C*, 2013, **117**, 17666–17673, DOI: 10.1021/jp405625x.

27 V. Maurice, M. Salmeron and G. Somorjai, The epitaxial growth of zirconium oxide thin films on Pt(111) single crystal surfaces, *Surf. Sci.*, 1990, **237**, 116–126, DOI: 10.1016/0039-6028(90)90524-C.

28 K. Meinel, A. Eichler, S. Förster, K.-M. Schindler, H. Neddermeyer and W. Widdra, Surface and interface structures of epitaxial ZrO_2 films on Pt(111): Experiment and density-functional theory calculations, *Phys. Rev. B*, 2006, **74**, 235444, DOI: 10.1103/PhysRevB.74.235444.

29 P. Lackner, J. I. J. Choi, U. Diebold and M. Schmid, Construction and evaluation of an ultrahigh-vacuum-compatible sputter deposition source, *Rev. Sci. Instrum.*, 2017, **88**, 103904, DOI: 10.1063/1.4998700.

30 L. Mayr, N. Köpfle, A. Auer, B. Klötzer and S. Penner, An (ultra) high-vacuum compatible sputter source for oxide thin film growth, *Rev. Sci. Instrum.*, 2013, **84**, 094103, DOI: 10.1063/1.4821148.

31 V. Maurice, K. Takeuchi, M. Salmeron and G. A. Somorjai, The bonding of diethyl ether, ethanol and their fluorinated analogs to zirconium oxide thin films, *Surf. Sci.*, 1991, **250**, 99–111, DOI: 10.1016/0039-6028(91)90713-3.

32 K. Takeuchi, S. S. Perry, M. Salmeron and G. A. Somorjai, The bonding properties of hydrogenated and fluorinated molecules to zirconium oxide thin films: influence of surface defects and water coadsorption, *Surf. Sci.*, 1995, **323**, 30–38, DOI: 10.1016/0039-6028(94)00621-0.

33 M. Antlanger, W. Mayr-Schmölzer, J. Pavelec, F. Mittendorfer, J. Redinger, P. Varga, U. Diebold and M. Schmid, Pt_3Zr(0001): A substrate for growing well-ordered ultrathin zirconia films by oxidation, *Phys. Rev. B*, 2012, **86**, 035451, DOI: 10.1103/PhysRevB.86.035451.

34 J. I. J. Choi, W. Mayr-Schmölzer, I. Valenti, P. Luches, F. Mittendorfer, J. Redinger, U. Diebold and M. Schmid, Metal adatoms and clusters on ultrathin zirconia films, *J. Phys. Chem. C*, 2016, **120**, 9920–9932, DOI: 10.1021/acs.jpcc.6b03061.

35 J. I. J. Choi, W. Mayr-Schmölzer, F. Mittendorfer, J. Redinger, U. Diebold and M. Schmid, The growth of ultra-thin zirconia films on $Pd_3Zr(0001)$, *J. Phys.: Condens. Matter*, 2014, **26**, 225003, DOI: 10.1088/0953-8984/26/22/225003.

36 H. Li, J.-I. J. Choi, W. Mayr-Schmölzer, C. Weilach, C. Rameshan, F. Mittendorfer, J. Redinger, M. Schmid and G. Rupprechter, Growth of an ultrathin zirconia film on Pt_3Zr examined by high-resolution X-ray photoelectron spectroscopy, temperature-programmed desorption, scanning tunneling microscopy, and density functional theory, *J. Phys. Chem. C*, 2015, **119**, 2462–2470, DOI: 10.1021/jp5100846.

37 J. Pavelec, J. Hulva, D. Halwidl, R. Bliem, O. Gamba, Z. Jakub, F. Brunbauer, M. Schmid, U. Diebold and G. S. Parkinson, A multi-technique study of CO_2 adsorption on Fe_3O_4 magnetite, *J. Chem. Phys.*, 2017, **146**, 014701, DOI: 10.1063/1.4973241.

38 E.-M. Köck, M. Kogler, R. Pramsoler, B. Klötzer and S. Penner, A high-temperature, ambient-pressure ultra-dry operando reactor cell for Fourier-transform infrared spectroscopy, *Rev. Sci. Instrum.*, 2014, **85**, 084102, DOI: 10.1063/1.4891630.

39 G. Kresse and D. Joubert, From ultrasoft pseudopotentials to the projector augmented-wave method, *Phys. Rev. B*, 1999, **59**, 1758–1775, DOI: 10.1103/PhysRevB.59.1758.

40 J. Carrasco, A. Hodgson and A. Michaelides, A molecular perspective of water at metal interfaces, *Nat. Mater.*, 2012, **11**, 667–674, DOI: 10.1038/nmat3354.

41 J. Carrasco, J. Klimeš and A. Michaelides, The role of van der Waals forces in water adsorption on metals, *J. Chem. Phys.*, 2013, **138**, 024708, DOI: 10.1063/1.4773901.

42 J. Klimeš, D. Bowler and A. Michaelides, van der Waals density functionals applied to solids, *Phys. Rev. B*, 2011, **83**, 1–13, DOI: 10.1103/PhysRevB.83.195131.

43 J. Klimeš, D. R. Bowler and A. Michaelides, Chemical accuracy for the van der Waals density functional, *J. Phys.: Condens. Matter*, 2010, **22**, 022201, DOI: 10.1088/0953-8984/22/2/022201.

44 M. Dion, H. Rydberg, E. Schröder, D. C. Langreth and B. I. Lundqvist, van der Waals density functional for general geometries, *Phys. Rev. Lett.*, 2004, **92**, 22–25, DOI: 10.1103/PhysRevLett.92.246401.

45 J. Tersoff and D. Hamann, Theory and application for the scanning tunneling microscope, *Phys. Rev. Lett.*, 1983, **50**, 1998, DOI: 10.1103/PhysRevLett.50.1998.

46 L. Köhler and G. Kresse, Density functional study of CO on Rh(111), *Phys. Rev. B*, 2004, **70**, 1–9, DOI: 10.1103/PhysRevB.70.165405.

47 G. Henkelman and H. Jónsson, A dimer method for finding saddle points on high dimensional potential surfaces using only first derivatives, *J. Chem. Phys.*, 1999, **111**, 7010–7022, DOI: 10.1063/1.480097.

48 A. Heyden, A. T. Bell and F. J. Keil, Efficient methods for finding transition states in chemical reactions: Comparison of improved dimer method and partitioned rational function optimization method, *J. Chem. Phys.*, 2005, **123**, 224101, DOI: 10.1063/1.2104507.

49 A. M. de Jong and J. W. Niemantsverdriet, Thermal desorption analysis: Comparative test of ten commonly applied procedures, *Surf. Sci.*, 1990, **233**, 355–365, DOI: 10.1016/0039-6028(90)90649-S.

50 E. Habenschaden and J. Küppers, Evaluation of flash desorption spectra, *Surf. Sci.*, 1984, **138**, L147–L150, DOI: 10.1016/0039-6028(84)90488-6.

51 L. Chaix, H. van den Bergh and M. J. Rossi, Real-time kinetic measurements of the condensation and evaporation of D_2O molecules on ice at 140 K < T < 220 K, *J. Phys. Chem. A*, 1998, **102**, 10300–10309, DOI: 10.1021/jp983050n.

52 Z. Dohnálek, G. A. Kimmel, S. A. Joyce, P. Ayotte, R. S. Smith and B. D. Kay, Physisorption of CO on the MgO(100) surface, *J. Phys. Chem. B*, 2001, **105**, 3747–3751, DOI: 10.1021/jp003174b.

53 M. Setvín, M. Buchholz, W. Hou, C. Zhang, B. Stöger, J. Hulva, T. Simschitz, X. Shi, J. Pavelec, G. S. Parkinson, M. Xu, Y. Wang, M. Schmid, C. Wöll, A. Selloni and U. Diebold, A multitechnique study of CO adsorption on the TiO_2 anatase(101) Surface, *J. Phys. Chem. C*, 2015, **119**, 21044–21052, DOI: 10.1021/acs.jpcc.5b07999.

54 S. L. Tait, Z. Dohnálek, C. T. Campbell and B. D. Kay, n-alkanes on MgO(100). I. Coverage-dependent desorption kinetics of n-butane, *J. Chem. Phys.*, 2005, **122**, 164707, DOI: 10.1063/1.1883629.

55 D. Halwidl, B. Stöger, W. Mayr-Schmölzer, J. Pavelec, D. Fobes, J. Peng, Z. Mao, G. S. Parkinson, M. Schmid, F. Mittendorfer, J. Redinger and U. Diebold, Adsorption of water at the SrO surface of ruthenates, *Nat. Mater.*, 2016, **15**, 450–455, DOI: 10.1038/nmat4512.

56 V. Coustet and J. Jupille, Hydroxyl groups on oxide surfaces, *Nuovo Cimento D*, 1997, **19**, 1657–1664, DOI: 10.1007/BF03185360.

57 M. Wagner, P. Lackner, S. Seiler, A. Brunsch, R. Bliem, S. Gerhold, Z. Wang, J. Osiecki, K. Schulte, L. A. Boatner, M. Schmid, B. Meyer and U. Diebold, Resolving the structure of a well-ordered hydroxyl overlayer on $In_2O_3(111)$: Nanomanipulation and theory, *ACS Nano*, 2017, **11**, 11531–11541, DOI: 10.1021/acsnano.7b06387.

58 S. J. Kerber, J. J. Bruckner, K. Wozniak, S. Seal, S. Hardcastle and T. L. Barr, The nature of hydrogen in x-ray photoelectron spectroscopy: General patterns from hydroxides to hydrogen bonding, *J. Vac. Sci. Technol., A*, 1996, **14**, 1314–1320, DOI: 10.1116/1.579947.

59 W. Smekal, W. S. M. Werner and C. J. Powell, Simulation of electron spectra for surface analysis (SESSA): a novel software tool for quantitative Auger-electron spectroscopy and X-ray photoelectron spectroscopy, *Surf. Interface Anal.*, 2005, **37**, 1059–1067, DOI: 10.1002/sia.2097.

60 G. A. Kimmel, M. Persson, Z. Dohnálek and B. D. Kay, Temperature independent physisorption kinetics and adsorbate layer compression for Ar adsorbed on Pt(111),

J. Chem. Phys., 2003, **119**, 6776–6783, DOI: 10.1063/1.1604111.

61 J. Hulva, Z. Jakub, Z. Novotny, N. Johansson, J. Knudsen, J. Schnadt, M. Schmid, U. Diebold and G. S. Parkinson, Adsorption of CO on the Fe_3O_4(001) surface, *J. Phys. Chem. B*, 2018, **122**, 721–729, DOI: 10.1021/acs.jpcb.7b06349.

62 M. A. Henderson, Evidence for bicarbonate formation on vacuum annealed TiO_2(110) resulting from a precursor-mediated interaction between CO_2 and H_2O, *Surf. Sci.*, 1998, **400**, 203–219, DOI: 10.1016/S0039-6028(97)00863-7.

63 J. Tennyson, P. F. Bernath, L. R. Brown, A. Campargue, A. G. Császár, L. Daumont, R. R. Gamache, J. T. Hodges, O. V. Naumenko, O. L. Polyansky, *et al.*, IUPAC critical evaluation of the rotational–vibrational spectra of water vapor, Part III: Energy levels and transition wavenumbers for, *J. Quant. Spectrosc. Radiat. Transfer*, 2013, **117**, 29–58, DOI: 10.1016/j.jqsrt.2012.10.002.

64 F. C. Jentoft, J. Kröhnert, I. R. Subbotina and V. B. Kazansky, Quantitative analysis of IR intensities of alkanes adsorbed on solid acid catalysts, *J. Phys. Chem. C*, 2013, **117**, 5873–5881, DOI: 10.1021/jp4004856.

65 S. T. Korhonen, M. Calatayud and A. O. I. Krause, Stability of Hydroxylated $(\bar{1}11)$ and $(\bar{1}01)$ surfaces of monoclinic zirconia: A combined study by DFT and infrared spectroscopy, *J. Phys. Chem. C*, 2008, **112**, 6469–6476, DOI: 10.1021/jp8008546.

66 K. T. Jung and A. T. Bell, The effects of synthesis and pretreatment conditions on the bulk structure and surface properties of zirconia, *J. Mol. Catal. A: Chem.*, 2000, **163**, 27–42, DOI: 10.1016/S1381-1169(00)00397-6.

67 M. W. Chase, *NIST-JANAF thermochemical tables*, American Chemical Society, American Institute of Physics for the National Institute of Standards and Technology, Washington, D.C., Woodbury, N.Y., 1998.

68 G. P. Johari, Configurational and vibrational entropies and molecular relaxation in supercooled water, *J. Chem. Phys.*, 2000, **112**, 10957–10965, DOI: 10.1063/1.481735.

69 S. Raz, K. Sasaki, J. Maier and I. Riess, Characterization of adsorbed water layers on Y_2O_3-doped ZrO_2, *Solid State Ionics*, 2001, **143**, 181–204, DOI: 10.1016/S0167-2738(01)00826-8.

70 A. R. Puigdollers and G. Pacchioni, Reducibility of ZrO_2/Pt_3Zr and ZrO_2/Pt 2D films compared to bulk zirconia: a DFT+U study of oxygen removal and H_2 adsorption, *Nanoscale*, 2017, **9**, 6866–6876, DOI: 10.1039/C7NR01904A.

71 E. Whalley, The difference in the intermolecular forces of H_2O and D_2O, *Trans. Faraday Soc.*, 1957, **53**, 1578–1585, DOI: 10.1039/TF9575301578.

72 W. Piskorz, J. Gryboś, F. Zasada, S. Cristol, J.-F. Paul, A. Adamski and Z. Sojka, Periodic DFT and atomistic thermodynamic modeling of the surface hydration equilibria and morphology of monoclinic ZrO_2 nanocrystals, *J. Phys. Chem. C*, 2011, **115**, 24274–24286, DOI: 10.1021/jp2086335.

73 J. K. Dewhurst and J. E. Lowther, Relative stability, structure, and elastic properties of several phases of pure zirconia, *Phys. Rev. B*, 1998, **57**, 741–747, DOI: 10.1103/PhysRevB.57.741.

74 A. Christensen and E. A. Carter, First-principles study of the surfaces of zirconia, *Phys. Rev. B*, 1998, **58**, 8050–8064, DOI: 10.1103/PhysRevB.58.8050.

75 M. Setvín, M. Wagner, M. Schmid, G. S. Parkinson and U. Diebold, Surface point defects on bulk oxides: atomically-resolved scanning probe microscopy, *Chem. Soc. Rev.*, 2017, **46**, 1772–1784, DOI: 10.1039/c7cs00076f.

76 G. Tzvetkov, Y. Zubavichus, G. Koller, T. Schmidt, C. Heske, E. Umbach, M. Grunze, M. Ramsey and F. Netzer, Growth of H_2O layers on an ultra-thin Al_2O_3 film: from monomeric species to ice, *Surf. Sci.*, 2003, **543**, 131–140, DOI: 10.1016/S0039-6028(03)01029-X.

77 C.-W. Yi and J. Szanyi, D_2O adsorption on an ultrathin alumina film on NiAl(110), *J. Phys. Chem. C*, 2007, **111**, 17597–17602, DOI: 10.1021/jp074459s.

78 J. L. Daschbach, Z. Dohnálek, S.-R. Liu, R. S. Smith and B. D. Kay, Water adsorption, desorption, and clustering on FeO(111), *J. Phys. Chem. B*, 2005, **109**, 10362–10370, DOI: 10.1021/jp058013s.

79 G. Kresse, M. Schmid, E. Napetschnig, M. Shishkin, L. Köhler and P. Varga, Structure of the ultrathin aluminum oxide film on NiAl(110), *Science*, 2005, **308**, 1440–1442, DOI: 10.1126/science.1107783.

80 D. R. Mullins, The surface chemistry of cerium oxide, *Surf. Sci. Rep.*, 2015, **70**, 42–85, DOI: 10.1016/j.surfrep.2014.12.001.

81 G. Pacchioni, L. Giordano and M. Baistrocchi, Charging of metal atoms on ultrathin MgO/Mo(100) films, *Phys. Rev. Lett.*, 2005, **94**, 226104, DOI: 10.1103/PhysRevLett.94.226104.

82 M. Sterrer, T. Risse, M. Heyde, H.-P. Rust and H.-J. Freund, Crossover from three-dimensional to two-dimensional geometries of Au nanostructures on thin MgO(001) films: A confirmation of theoretical predictions, *Phys. Rev. Lett.*, 2007, **98**, 206103, DOI: 10.1103/PhysRevLett.98.206103.